

1

Fog and Rain in the Amazon

2 Usama Anber ^{a,b,1}, Pierre Gentine ^{c,1}, Shuguang Wang ^d, and Adam Sobel ^{a,b,d}

3

^a Lamont-Doherty Earth Observatory of Columbia University, Palisades, NY

^b Department of Earth and Environmental Sciences, Columbia University, New York, NY

^c Department of Earth and Environmental Engineering and Earth Institute, Columbia University, New York, NY

^d Department of Applied Physics and Applied Mathematics, Columbia University, New York, NY

¹ To whom correspondence may be addressed. E-mail: uanber@ldeo.columbia.edu or pg2328@columbia.edu

Authors contributions: U.A. and P.G. designed research; U.A., P.G., and S.W. performed research; U.A., P.G., S.W., and A.S. wrote the paper.

4 **Abstract**

5 The diurnal and seasonal water cycles in the Amazon remain poorly simulated in
6 general circulation models, exhibiting peak evapotranspiration in the wrong season and
7 rain too early in the day. We show that those biases are not present in cloud-resolving
8 simulations with parameterized large-scale circulation. The difference is attributed to the
9 representation of the morning fog layer, and to more accurate characterization of
10 convection and its coupling with large-scale circulation. The morning fog layer, present
11 in the wet season but absent in the dry, dramatically increases cloud albedo, which
12 reduces evapotranspiration through its modulation of the surface energy budget. These
13 results highlight the importance of the coupling between the energy and hydrological
14 cycles and the key role of cloud albedo feedback for climates over tropical continents.

15 **Significance Statement**

16 We here demonstrate that we can resolve the seasonality of the hydrologic cycle in the
17 Amazon using an approach opposite to general circulation models, in which we resolve
18 convection and parameterize large-scale circulation as a function of the resolved
19 convection. The results emphasize the key role of cloud albedo feedback and in particular
20 of the morning fog layer in determining the diurnal course of surface heat fluxes and
21 seasonality of the surface and atmospheric heat and water cycles. These results indicate
22 that our understanding of tropical climates over land can be considerably advanced by
23 using coupled land-atmosphere models with explicit convection and parameterized large-
24 scale dynamics.

25

26 **\body**

27 **Introduction**

28 Tropical forests, and the Amazon in particular, are the biggest terrestrial CO₂
29 sinks on the planet, accounting for about 30% of the total net primary productivity in
30 terrestrial ecosystems. Hence, the climate of the Amazon is of particular importance for
31 the fate of global CO₂ concentration in the atmosphere (1). Besides the difficulty of
32 estimating carbon pools (1-3), our incapacity to correctly predict CO₂ fluxes in the
33 continental tropics largely results from inaccurate simulation of the tropical climate (1, 2,
34 4, 5). More frequent and more intense droughts in particular are expected to affect the
35 future health of the Amazon and its capacity to act as a major carbon sink (6-8). The land
36 surface is not isolated, though, but interacts with the weather and climate through a series
37 of land-atmosphere feedback loops, which couples the energy, carbon and water cycles
38 through stomata regulation and boundary layer mediation (9).

39 Current General Circulation Models (GCMs) fail to correctly represent some of
40 the key features of the Amazon climate. In particular, they i) underestimate the
41 precipitation in the region (10, 11), ii) do not reproduce the seasonality of either
42 precipitation (10, 11) or surface fluxes such as evapotranspiration (12), and iii) produce
43 errors in the diurnal cycle and intensity of precipitation, with a tendency to rain too little
44 and too early in the day (13, 14). In the more humid Western part of the basin, surface
45 incoming radiation, evapotranspiration, and photosynthesis all tend to peak in the dry
46 season (15-17) whereas GCMs simulate peaks of those fluxes in the wet season (10, 11).
47 Those issues might be related to the representation of convection (1, 2, 4, 5, 13, 14) and
48 vegetation water stress (6-8, 15-17) in GCMs.

49 We here show that we can represent the Amazonian climate using a strategy
50 opposite to GCMs in which we resolve convection and parameterize the large-scale
51 circulation (Methods). The simulations lack many of the biases observed in GCMs and
52 more accurately capture the differences between the dry and wet season of the Amazon in
53 surface heat fluxes and precipitation. Besides top of the atmosphere insolation, the
54 simulations require the monthly-mean temperature profile as an input. We demonstrate
55 that this profile, whose seasonal cycle itself is a product of the coupled ocean-land-
56 atmosphere dynamics, mediates the seasonality of the Amazonian climate by modulating
57 the vertical structure of the large-scale circulation in such a way that thermal energy is
58 less effectively ventilated in the rainy season.

59 **Results and Discussion**

60 We use the Weather Research and Forecasting (WRF) model at 2km horizontal
61 grid spacing (see methods section for details of the runs). This resolution has been shown
62 to be sufficient to resolve deep convection (no convective parameterization is used) and
63 to correctly represent the sign and magnitude of the land-atmosphere interaction feedback
64 (*18*) contrary to GCMs, which tend to exhibit soil moisture-precipitation feedbacks of
65 opposite sign to that observed (*19*). We parameterize the time-dependent large-scale
66 vertical motion as a function of internally resolved convection using the weak
67 temperature gradient (WTG) approximation (Methods). The WTG approach has been
68 used in many previous studies of tropical atmospheric dynamics to represent the feedback
69 between locally resolved convection and larger-scale circulation (Methods) (*10, 11, 20-*
70 *23*). Under WTG, we diagnose the horizontal-average large-scale vertical motion (Fig.
71 S1) so as to induce a vertical advective potential temperature tendency, which relaxes the

72 model's domain-averaged potential temperature towards that of the target profile. The
73 same large-scale vertical motion is then also used for vertical advection of moisture
74 (Methods).

75 The target potential temperature profiles we use, representative of the wetter part
76 of the Amazon, are taken from the 2014 Atmospheric Radiation Measurement (ARM)
77 mobile facility located at Manacapuru, near Manaus, Brazil ($3^{\circ} 12' 46.70''$ S, $60^{\circ} 35'$
78 $53.0W$). The profiles are averaged over the month of February for the wet season, and
79 September for the dry season, as shown in Fig. 1a. At the surface (where WTG is not
80 directly applied, see methods) the dry profile is warmer by about 5K, reflecting the
81 influence of higher surface heat fluxes (Fig. 1b). In the mid-troposphere the wet profile is
82 warmer by more than 1K. In the stratosphere, the wet profile is colder by more than 5K
83 due to the seasonal elevation of the tropopause. All these differences are consequences of
84 the seasonal cycle itself; the warmer troposphere and cooler lower stratosphere are typical
85 differences between states of stronger and weaker deep convection (24). Here the
86 ultimate cause of the wet-dry season temperature difference is presumably the stronger
87 insolation in the wet season, but the temperature differences are in part an outcome of
88 land-atmosphere interactions, as the tropospheric temperature difference between the two
89 seasons in the nearby oceanic regions shows no such signal (Fig. S2). Since we assume
90 this seasonal difference in temperature profiles, our simulations do not predict the
91 seasonal changes purely as a function of external boundary conditions and forcing.
92 Rather, we predict part of the solution – including precipitation, clouds, and surface
93 fluxes – given another, the free atmospheric temperature. This allows us to understand
94 the mediation of convection and land-atmosphere interaction by the atmospheric

95 temperature, similar to what has been done in studies of tropical cyclones and the
96 Madden-Julian oscillation (24,29) .

97 The increase in precipitation in the wet season relative to the dry (Fig. 2) can be
98 attributed to the reduction in the export of moist static energy by the large-scale
99 circulation (See supplementary materials) which is a consequence of the more stable
100 temperature profile (29), despite the absence of an increase in surface fluxes or radiative
101 heating. This increase, in turn, moistens the land surface, an important factor leading to
102 the differences in cloud between the wet and dry seasons. In agreement with observations
103 (here CPC Morphing Technique (CMORPH) (27) data averaged over 10 years (2004-
104 2014) for the month of February and September for the wet and dry seasons,
105 respectively), our simulated precipitation maxima occur in the early to late afternoon in
106 both seasons, with greater absolute amplitude in the wet season.

107 In both seasons, rapid precipitation transitions from minima in the morning local
108 hours to maxima in the afternoon are associated with transitions from shallow to deep
109 convection (Fig. 3). In the dry season (Fig. 3a), convection starts in the morning (10 a.m.
110 time-zone local time) manifesting first as a sharp increase in midlevel cloud at that time
111 coverage, and then a more gradual transition to deep convection in the afternoon
112 associated with the timing of rainfall maxima. Midlevel cloud cover dissipates overnight
113 into the early morning. The overall cloud cover is relatively small during daytime, and
114 higher in the afternoon and evening, as observed, but contrary to what GCMs predict as
115 mentioned above. The smaller cloud cover during daytime drives greater surface fluxes,
116 and in particular evapotranspiration and photosynthesis, by allowing more solar radiation
117 to reach the surface.

118 In the wet season (Fig. 3b), the diurnal cycle of cloud cover exhibits a different
119 behavior. In addition to the increase in cloud cover, there is now a distinct layer of fog
120 above the surface that is maintained by radiative cooling from the wet surface and lasts
121 from midnight until noon, as observed in the Amazon (Fig.S3 and S4) and other
122 rainforests. This morning fog layer blocks shortwave radiation from reaching the surface
123 and reduces daytime net surface shortwave radiation and evapotranspiration. Such
124 morning fog was also shown to be critical in the maintenance of distinct diurnal climate
125 equilibrium regimes by a previous modeling study (25, 26).

126 As a result, the latent heat flux (Fig. 4a) and surface temperature are smaller in the
127 wet season than in the dry season, because surface shortwave radiation is reduced by the
128 fog layer (Fig. 4b), which more than compensates for the higher soil water availability
129 and lower Bowen ratio in the wet season (from diurnal average of 0.4 in the dry season to
130 0.32 in the wet season based on eddy-covariance data). We note that surface observations
131 have difficulty observing in the presence of dew (eddy-covariance measurements cannot
132 correctly record measurements) so that most days with fog are not captured by surface
133 observations; thus clear days (infrequent in the wet season – Fig S3 and S4) with higher
134 latent heat flux are overrepresented in the observations. As the diurnal rise of the surface
135 turbulent fluxes is delayed in the wet season by the fog layer the transition from shallow
136 to deep convection occurs later in the day compared to the dry season.

137 Although the downward solar insolation at the top of the atmosphere in the wet
138 season exceeds that in the dry season by more than 20 Wm^{-2} , the net shortwave radiation
139 at the surface is greater in the dry season (Fig. 4b). This results from a strong negative
140 cloud albedo feedback in the wet season and greater reflection of shortwave radiation to

141 space. The fog layer is an important contributor to this albedo. We further quantify the
142 cloud-albedo feedback by computing cloud radiative forcing (CRF), as the clear sky
143 minus all-sky upwelling flux at the top of the atmosphere (Fig. 5). Weaker convection in
144 the dry season induces a smaller longwave CRF component compared to that induced in
145 the wet season. However, the shortwave CRF in the wet season is much more negative
146 than in the dry season due to the presence of the fog layer. Because the shortwave CRF
147 dominates in the wet season, and longwave CRF dominates in the dry season, the net
148 CRF is negative in the wet season and positive in the dry. Comparison with CRF obtained
149 from the CERES (the CERES SYN1deg daily radiative fluxes: Clouds and the Earth's
150 Radiant Energy System; 30, 31) shows a reasonable agreement with our simulations,
151 although some biases exist.

152 Perhaps surprisingly, the seasonal difference in the top of the atmosphere seasonal
153 mean insolation is not the dominant control that determines the differences in seasonal
154 climate, even though it is ultimately what controls the seasonal cycle in nature. In our
155 simulations, the differences in the target potential temperature profiles are primarily
156 responsible for the seasonal differences described above. We performed sensitivity
157 experiments in which the insolation from the wet season is used with the target potential
158 temperature profile from the dry season and vice versa (see supplementary figures – Fig.
159 S5 to S7). We also performed sensitivity experiments over Rondonia (10.7 *S*, 62.7 *W*),
160 where the seasonal difference in insolation is greater (supplementary figures – Fig. S8 to
161 S10). When insolation is varied while holding the potential temperature profile fixed, no
162 significant difference is found in terms of the typical pattern of diurnal and seasonal
163 patterns of precipitation. Again, the cloud albedo adjusts so that the surface shortwave

164 radiation is always higher in the case of the dry season profile, leading to higher
165 evapotranspiration flux (Fig. S9). This behavior differs from convection over oceans,
166 where stronger seasonal insolation leads to higher surface fluxes (and sea surface
167 temperature), and cloud albedo is not so tightly coupled to atmospheric convection
168 because, unlike land, the ocean can both substantially store and transport heat reducing
169 the coupling of evaporation with shortwave incoming radiation.

170 **Methods**

171 **Model configuration:**

172 We use the Weather Research and Forecast (WRF) model version 3.3, in three spatial
173 dimensions, with doubly periodic lateral boundary conditions. The experiments are
174 conducted with Coriolis parameter $f = 0$. The horizontal domain size is $192 \times 192 \text{ km}^2$
175 with a grid spacing of 2 km. There are 50 vertical levels total, with the top level at 22 km,
176 and 10 levels in the lowest 1 km. Gravity waves propagating vertically are absorbed in
177 the top 5 km to prevent unphysical wave reflection off the top boundary by using the
178 implicit damping vertical velocity scheme (32). The 2-Dimensional Smagorinsky first
179 order turbulent closure scheme is used to parameterize the horizontal transports by sub-
180 grid eddies. The Yonsei University (YSU) first order closure scheme is used to
181 parameterize non-local boundary layer turbulence and vertical subgrid-scale eddy
182 diffusion (33). The surface fluxes of moisture and heat are parameterized following
183 Monin-Obukhov similarity theory. Microphysics is simulated using the Purdue-Lin bulk
184 scheme (34) which has six species: water vapor, cloud water, cloud ice, rain, snow, and
185 graupel. Radiative fluxes are determined interactively using the NCAR Community

186 Atmosphere Model (CAM 3.0) scheme for shortwave and longwave radiation. Both
187 surface and radiative fluxes are fully interactive.

188 The atmospheric model is coupled to the Noah land surface model (LSM) (35)
189 that has four soil layers at 10, 30, 60, and 100 cm depth. The LSM provides four
190 quantities to the atmospheric model: sensible heat flux, latent heat flux, upward longwave
191 radiation, and upward shortwave radiation off the ground. The LSM prognostic land
192 states are: surface skin temperature, volumetric total (liquid and frozen) soil moisture at
193 each layer, soil temperature at each layer, canopy water content. Vegetation type is
194 evergreen forest, surface albedo is 0.12, and the wind field is left un-nudged.

195

196 **Parameterized Large Scale Circulation and Initial Conditions:**

197 The large-scale vertical velocity is dynamically parameterized using the WTG method
198 (20, 21). The WTG vertical velocity W_{WTG} is obtained by a Newtonian relaxation with a
199 relaxation time scale τ (over which gravity waves propagate out of the domain) taken
200 here as 2 hours (20, 21):

$$201 \quad W_{\text{WTG}}(z) = \frac{1}{\tau} \frac{\bar{\theta} - \theta_0}{\partial \bar{\theta} / \partial z} \quad (1)$$

202 where $\bar{\theta}$ is the domain mean potential temperature, θ_0 is the observed potential
203 temperature profile obtained from radiosondes averaged over one month of observations.

204 W_{WTG} is then linearly interpolated in the boundary layer to zero at the surface since
205 gravity waves are not the main mode of buoyancy adjustment in the boundary layer. The
206 impact is negligible in the daytime boundary layer as it is well mixed so that the vertical

207 gradients are null. Boundary layer height is determined interactively in the WRF model
208 using the bulk Richardson number method and varies diurnally.

209 Once W_{WTG} is obtained, it is used to define the domain-average large-scale
210 tendencies of potential temperature and specific humidity over the computational domain:

$$211 \quad \frac{\partial \bar{\theta}}{\partial t} \Big|_{\text{Large Scale}} = -\frac{\bar{\theta} - \theta_0}{\tau}, \quad (2)$$

$$212 \quad \frac{\partial \bar{q}}{\partial t} \Big|_{\text{Large Scale}} = -W_{\text{WTG}} \frac{\partial \bar{q}}{\partial z}, \quad (3),$$

213 respectively, where \bar{q} is the domain mean water vapor mixing ratio.

214 Initial conditions are seasonally averaged quantities in the dry and wet seasons
215 using the ERA-Interim data set. The model is run for about 40 days and the analysis
216 conducted on the equilibrium part only, which is the last 30 days. We have performed a
217 sensitivity test on the soil moisture initial conditions, by switching the seasonal
218 magnitudes, and they had no influence on the results. The reference, target temperature
219 profile is time-independent in each season and does not include diurnal variations (21).
220 The modeled diurnal cycles of surface fluxes, clouds, and precipitation are driven solely
221 by the diurnal cycle of radiation at the top of the atmosphere. Daily mean insolation in
222 the dry season is held fixed at 415 Wm^{-2} and in the wet season at 439 Wm^{-2} , reflecting
223 values at Manacapuru.

224 **Surface observations:**

225 We used eddy-covariance data from the K34 station located in Estação Experimental de
226 Silvicultura Tropical $02^{\circ} 37' \text{ S}$, $60^{\circ} 09' \text{ W}$, located around 60km from Manaus. We have

227 used data from 2000 to 2006 available at ORNL.gov (Saleska et al. 2013
228 <http://dx.doi.org/10.3334/ORNLDAAC/1174>). We used quality-controlled eddy
229 covariance data, based on outliers comparison, wind speed (acceptable variation is two
230 standard deviation units from the linear regression), and unresponsive sensor checks.
231 Eddy-covariance measurements typically cannot correctly measure in the presence of
232 dew, thus fog conditions are under-sampled, which implies that the latent heat flux in Fig.
233 4 is an overestimate of the true latent heat flux (an average of fog conditions with little
234 radiation and non-fog conditions with higher radiation).

235 **Conclusion**

236 We have shown that, when given the top of the atmosphere insolation and the
237 monthly mean free-atmospheric temperature profile, the seasonal and diurnal cycles of
238 cloud, precipitation, and surface fluxes can be simulated by a limited-domain cloud-
239 resolving model with parameterized large-scale forcing without the biases commonly
240 found in global climate models.

241 We can view the seasonality in the Amazon as mediated by the atmospheric
242 temperature profile. That profile itself results from the stronger convection in the wet
243 season, but the increased wet-season precipitation in the model is still a nontrivial
244 prediction of the model. It can be explained by the reduced ventilation of moist static
245 energy from the column, which is a consequence of the warmer tropospheric temperature
246 profile in the wet season.

247 The surface fluxes, on the other hand, are strongly controlled by the diurnal cycle
248 of cloud albedo, and especially of wet season fog, which blocks shortwave radiation from

249 reaching the surface in the early morning. This fog is an essential regulator of the
250 Amazon climate.

251 We demonstrate that a high-resolution cloud-resolving model with parameterized
252 large-scale circulation offers a new window onto the dynamics of climate in the Amazon.
253 In future this approach may allow new insights into the Amazon's changes under
254 anthropogenic influence and the capacity of the basin to act as a CO₂ sink in the future.

255 **Acknowledgements:**

256 Pierre Gentine was supported by DOE grant GoAmazon and DE-FOA-0000885 on the
257 transition between shallow and deep convection. Usama Anber, Shuguang Wang and
258 Adam Sobel acknowledge support from the National Science Foundation under grant
259 AGS-1008847 and the Office of Naval Research under MURI grant (N00014-12-1-0911).
260 Pierre Gentine would like to thank Florian Cochard for preliminary radiosonde and
261 profile analysis. WRF experiments were performed on the YETI cluster at Columbia
262 University. Data profiles at the ARM site were obtained at
263 <http://www.arm.gov/sites/amf/mao/>. Surface flux observations were obtained at
264 <http://dx.doi.org/10.3334/ORNLDAAAC/1174>.

265

266

267 **References**

- 268 1. Achard F, Eva HD, Mayaux P, Stibig H-J, Belward A (2004) Improved estimates
269 of net carbon emissions from land cover change in the tropics for the 1990s.
270 *Global Biogeochem Cy* 18:1–11.
- 271 2. Hoffman FM et al. (2014) Causes and Implications of Persistent Atmospheric
272 Carbon Dioxide Biases in Earth System Models. *J Geophys Res-Biogeophys*:141–162.
- 273 3. Cai W et al. (2014) Improved Estimations of Gross Primary Production Using
274 Satellite-Derived Photosynthetically Active Radiation. *J Geophys Res-Biogeophys*:n/a–
275 n/a.
- 276 4. Todd-Brown KEO et al. (2013) Causes of variation in soil carbon simulations from
277 CMIP5 Earth system models and comparison with observations. *Biogeosciences*
278 10:1717–1736.
- 279 5. Cox PM et al. (2013) Sensitivity of tropical carbon to climate change constrained
280 by carbon dioxide variability. *Nature* 494:341–344.
- 281 6. Lee JE et al. (2013) Forest productivity and water stress in Amazonia:
282 observations from GOSAT chlorophyll fluorescence. *Proceedings of the Royal*
283 *Society B: Biological Sciences* 280:20130171–20130171.
- 284 7. Reichstein M et al. (2013) Climate Extremes and the Carbon Cycle. *Nature*
285 500:287–295.
- 286 8. Gatti LV et al. (2015) Drought sensitivity of Amazonian carbon balance revealed
287 by atmospheric measurements. *Nature* 506:76–80.
- 288 9. de Arellano JV-G, van Heerwaarden CC, Lelieveld J (2012) Modelled suppression
289 of boundary-layer clouds by plants in a CO₂-rich atmosphere. *Nat Geosci* 5:701–
290 704.
- 291 10. Pascale S, Lucarini V, Feng X, Porporato A, Hasson SU (2014) Analysis of
292 Rainfall Seasonality From Observations and Climate Models. *Climate*
293 *dynamics*:1–21.
- 294 11. Martins G, Randow von C, Sampaio G, Dolman AJ (2014) Precipitation in the
295 Amazon and its relationship with moisture transport and tropical Pacific and
296 Atlantic SST from the CMIP5 simulations. *HESS discussions*.
- 297 12. de Gonçalves LGG et al. (2013) Agricultural and Forest Meteorology. *Agr Forest*
298 *Meteorol* 182-183:111–127.
- 299 13. Dai A (2006) Precipitation characteristics in eighteen coupled climate models. *J*
300 *Climate* 19:4605–4630.

- 301 14. Bechtold P et al. (2014) Representing Equilibrium and Nonequilibrium Convection
302 in Large-Scale Models. *J Atmos Sci* 71:734–753.
- 303 15. Da Rocha HR et al. (2009) Patterns of water and heat flux across a biome gradient
304 from tropical forest to savanna in Brazil. *J Geophys Res* 114:G00B12.
- 305 16. Fisher JB et al. (2009) The land-atmosphere water flux in the tropics. *Global*
306 *Change Biol* 15:2694–2714.
- 307 17. Restrepo-Coupe N et al. (2013) Agricultural and Forest Meteorology. *Agr Forest*
308 *Meteorol* 182-183:128–144.
- 309 18. Taylor CM, Birch CE, Parker DJ, Dixon N, Guichard F, Nikulin, G and Lister
310 GMS (2013) Modelling soil moisture - precipitation feedbacks in the Sahel:
311 importance of spatial scale versus convective parameterization, *Geophys Res Lett*,
312 40(23), 6213–6218, doi:10.1002/2013GL058511.
- 313 19. Guillod, B. P., Orlowsky, B., Miralles, D. G., Teuling, A. J., & Seneviratne, S. I.
314 (2015). Reconciling spatial and temporal soil moisture effects on afternoon rainfall.
315 *Nature communications*, 6.
- 316 20. Anber U, Wang S, Sobel A (2014) Response of Atmospheric Convection to
317 Vertical Wind Shear: Cloud-System-Resolving Simulations with Parameterized
318 Large-Scale Circulation. Part I: Specified Radiative Cooling. *J Atmos Sci* 71:2976–
319 2993.
- 320 21. Wang S, Sobel AH, Kuang Z (2013) Cloud-resolving simulation of TOGA-
321 COARE using parameterized large-scale dynamics. *J Geophys Res-Atmos*
322 118:6290–6301.
- 323 22. Sobel AH, Bretherton CS (2003) Large-scale waves interacting with deep
324 convection in idealized mesoscale model simulations. *Tellus Series A-Dynamic*
325 *Meteorology And Oceanography* 55:45–60.
- 326 23. Sobel AH, Nilsson J, Polvani L (2001) The weak temperature gradient
327 approximation and balanced tropical moisture waves. *J Atmos Sci* 58:3650–3665.
- 328 24. Holloway CE, Neelin JD (2007) The Convective Cold Top and Quasi Equilibrium.
329 *J Atmos Sci* 64:1467–1487.
- 330 25. Ramos da Silva, R. and R. Avissar, 2006. The hydrometeorology of a deforested
331 region of the Amazon basin. *J. Hydromet.*, 7, 1028-1042.
332
- 333 26. Rochetin N, Lintner BR, Findell KL, Sobel AH, Gentine P (2014) Radiative
334 convective equilibrium over a land surface. *J Climate* 27:140612144016000.
- 335 27. Dirmeyer, P. A., B. A. Cash, J. L. Kinter III, T. Jung, L. Marx, M. Satoh, C. Stan,

- 336 H. Tomita, P. Towers, N. Wedi, D. Achuthavarier, J. M. Adams, E. L. Altshuler,
 337 B. Huang, E. K. Jin, and J. Manganello, 2011: Simulating the diurnal cycle of
 338 rainfall in global climate models: Resolution versus parameterization. *Clim. Dyn.*,
 339 DOI 10.1007/s00382-011-1127-9, 20 pp.
- 340 28. Joyce RA, Janowiak J, Arkin PA, Xie P (2004) CMORPH: A Method that
 341 Produces Global Precipitation Estimates from Passive Microwave and Infrared
 342 Data at High Spatial and Temporal Resolution. *Journal of hydrometeorology* 5:1–
 343 17.
- 344 29. Raymond DJ, Sessions SL (2007) Evolution of convection during tropical
 345 cyclogenesis. *Geophys Res Lett* 34: L06811.
- 346 30. Wielicki, B. A., B. R. Barkstrom, E. F. Harrison, R. B. Lee III, G. L. Smith, and J.
 347 E. Cooper, 1996: Clouds and the Earth’s Radiant Energy System (CERES): An
 348 earth observing system experiment. *Bull. Amer. Meteor. Soc.*, 77, 853–868,
 349 doi:10.1175/1520-0477(1996)077<0853:CATERE.2.0.CO;2.
- 350 31. Loeb, N. G., S. Kato, W. Su, T. Wong, F. G. Rose, D. R. Doelling, J. R. Norris,
 351 and X. Huang, 2012: Advances in understanding top-of-atmosphere radiation
 352 variability from satellite observations. *Surv. Geophys.*, 33, 359–385, doi:10.1007/
 353 s10712-012-9175-1.
- 354 32. Klemp JB, Dudhia J, Hassiotis AD (2008) An Upper Gravity-Wave Absorbing
 355 Layer for NWP Applications. *Mon Wea Rev* 136:3987–4004.
- 356 33. Hong S-Y, Pan H-L (1996) Nonlocal Boundary Layer Vertical Diffusion in a
 357 Medium-Range Forecast Model. *Mon Wea Rev* 124:2322–2339.
- 358 34. Chen S-H, SUN W-Y (2002) A One-dimensional Time Dependent Cloud Model. *J*
 359 *Meteorol Soc Jpn* 80:99–118.
- 360 35. Ek MB (2003) Implementation of Noah land surface model advances in the
 361 National Centers for Environmental Prediction operational mesoscale Eta model. *J*
 362 *Geophys Res* 108:8851.
- 363 36. Sobel, A. H. Simple Models of Ensemble-Averaged Precipitation and Surface
 364 Wind, Given the SST. *The Global Circulation of the Atmosphere, edited by T.*
 365 *Schneider and A. H. Sobel* 219–251 (2007).
 366
- 367 37. Neelin, J. D. & Held, I. M. Modeling tropical convergence based on the moist
 368 static energy budget. *Mon Wea Rev* **115**, 3–12 (1987).
 369
- 370 38. Raymond, Sessions, Sobel, and Fuchs, 2009: The mechanics of gross moist
 371 stability *Journal of Advances in Modeling Earth Systems*, **1**,
 372 doi:10.3894/JAMES.2009.1.9
- 373

374

375

376

377 **Figure Legends:**

378 Fig. 1. (a) Monthly mean observed atmospheric potential temperature profile in the wet
379 (February) and dry season (September) observed at Manacapuru, near Manaus, Brazil (3°
380 $12' 46.70''$ S, $60^{\circ} 35' 53.0W$) using radiosonde and used as reference profiles for the weak
381 temperature gradient method. (b) Atmospheric potential temperature difference between
382 the wet and dry seasons.

383

384 Fig. 2. Diurnal cycle of modeled (thick line) and observed (thin line) precipitation from
385 CPC MORPH along with one third of the standard deviation (shaded area) in the local
386 time zone.

387

388 Fig. 3. Composite of the WRF simulated 2-day cycle of fractional cloud cover for (a) the
389 wet and (b) dry season. Note the fog layer above the surface in the wet season.

390

391 Fig. 4. Diurnal cycle of (a) latent heat flux, and (b) net shortwave at the surface, for WRF
392 modeled (thick) and observed (thin) fluxes. Observed fluxes are taken from the
393 climatology of eddy-covariance fluxes observed at K34 station in Reserva Biológica do
394 Cuieiras. We note that surface observations have difficulty observing in the presence of

395 dew (eddy-covariance measurements typically cannot correctly record measurements) so
396 that the observations typically omit fog situations, with an overrepresentation of
397 relatively clear days compared to fog days.

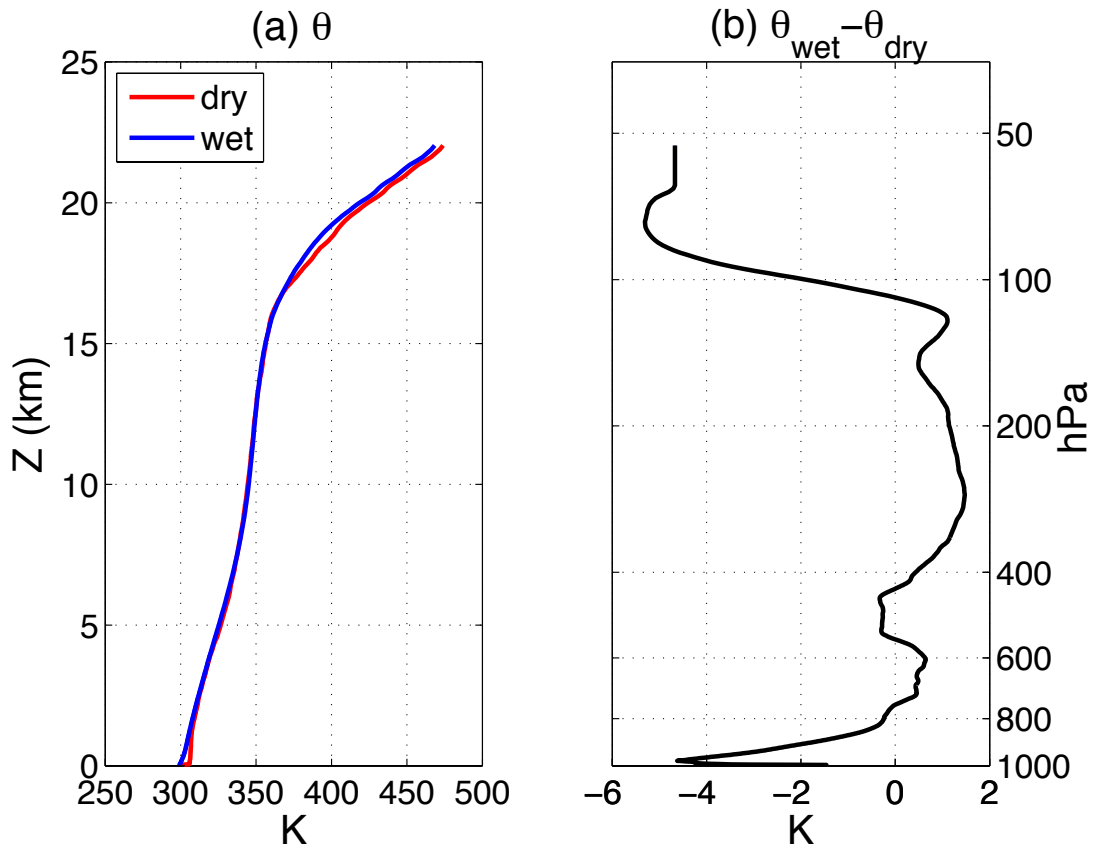
398

399 Fig. 5. Cloud radiative, shortwave (SWCRF), longwave (LWCRF), and net (NETCRF)
400 for the wet and dry seasons as simulated (in squares) and observed from CERES (in
401 circles).

402

403 **Figures**

404



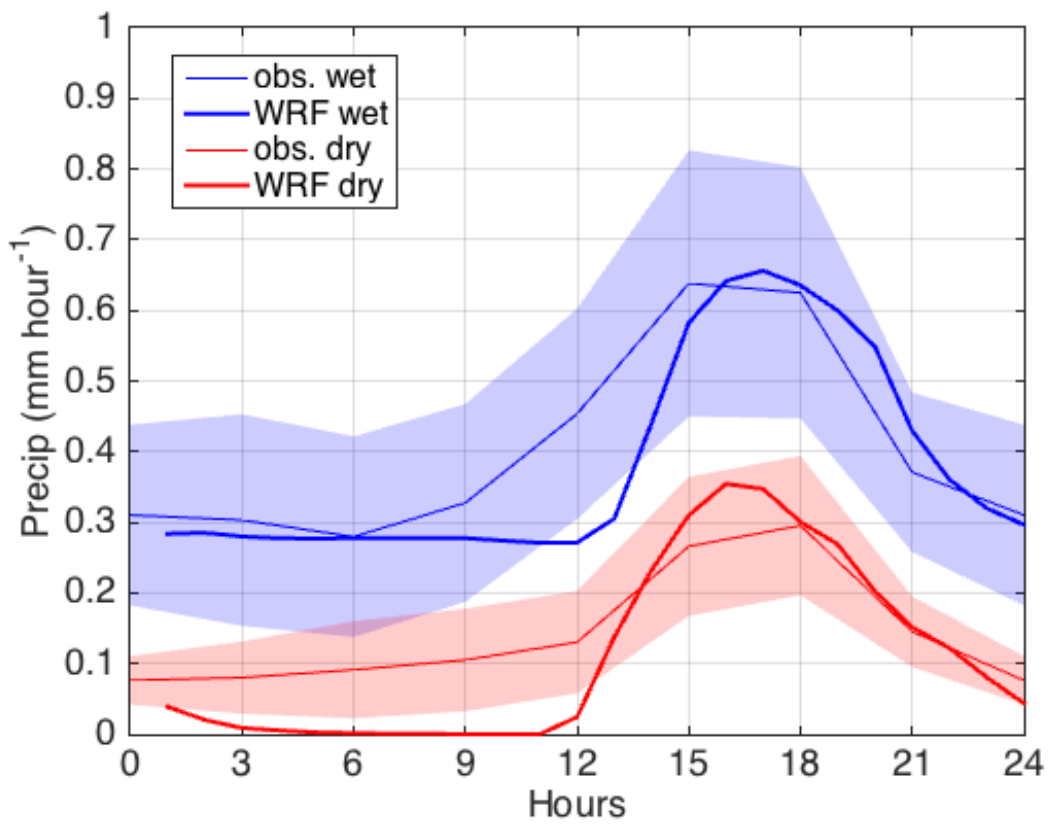
405

406 Fig. 1. (a) Monthly mean observed atmospheric potential temperature profile in the wet
407 (February) and dry season (September) observed at Manacapuru, near Manaus, Brazil (3°
408 12' 46.70" S, 60° 35' 53.0W) using radiosonde and used as reference profiles for the weak
409 temperature gradient method. (b) Atmospheric potential temperature difference between
410 the wet and dry seasons.

411

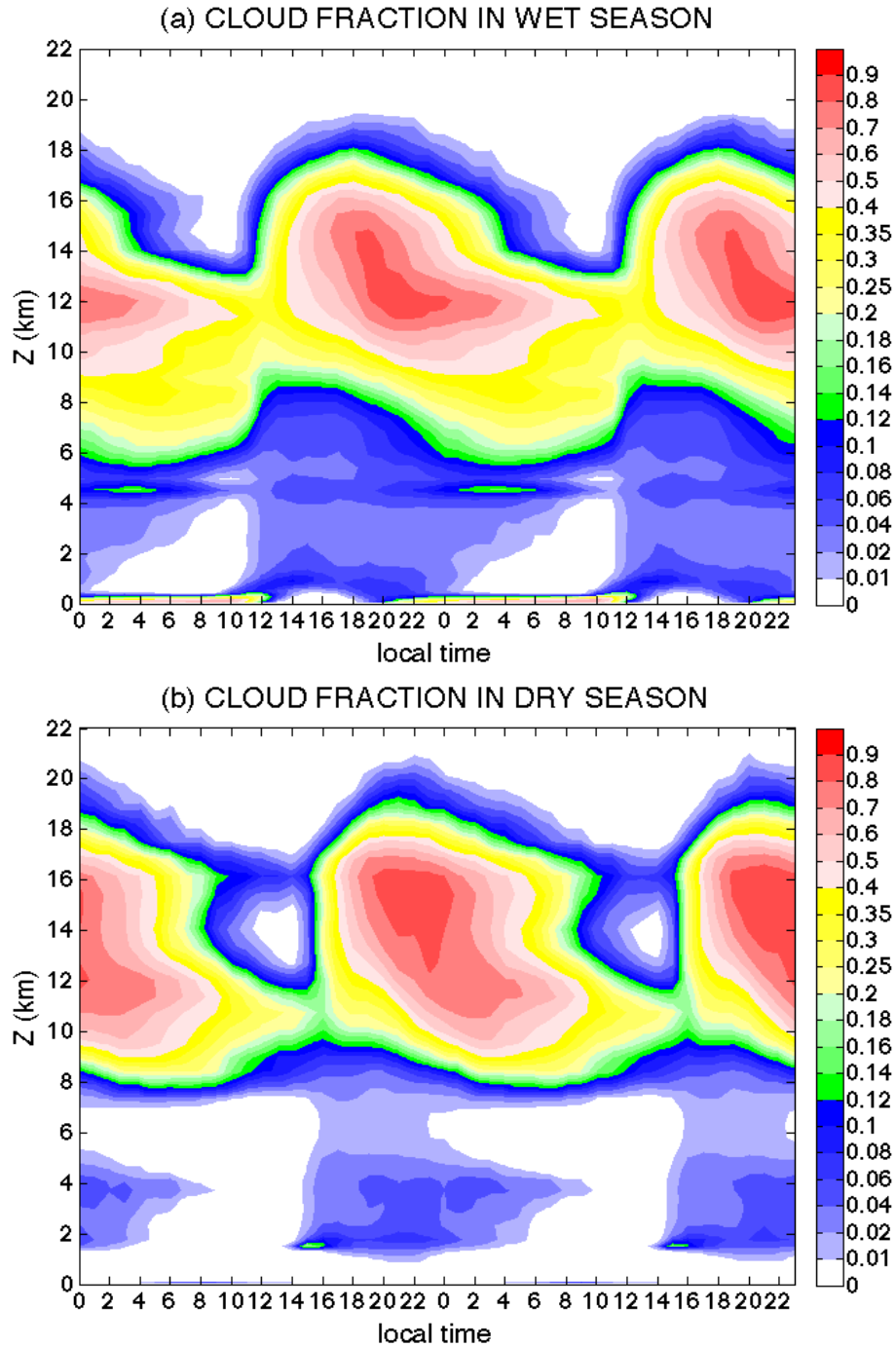
412

413
414
415
416
417
418
419



420
421
422
423
424

Fig. 2. Diurnal cycle of modeled (thick line) and observed (thin line) precipitation from CPC MORPH along with one third of the standard deviation (shaded area) in the local time zone.



425

426 Fig. 3. Composite of the WRF simulated 2-day cycle of fractional cloud cover for (a) the
 427 wet and (b) dry season in the local time zone. Note the fog layer above the surface in the
 428 wet season.

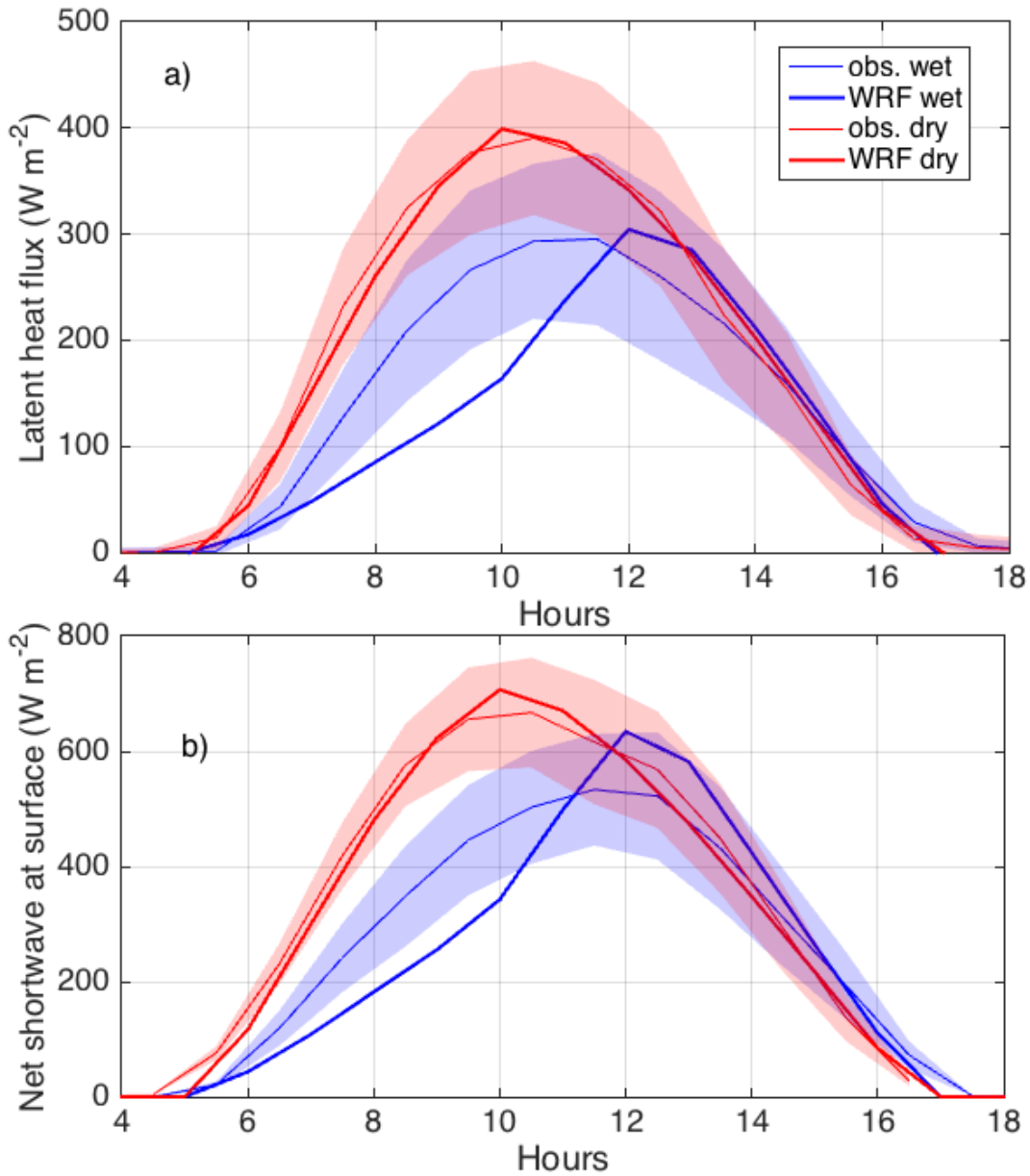
429

430

431

432

433
434



435

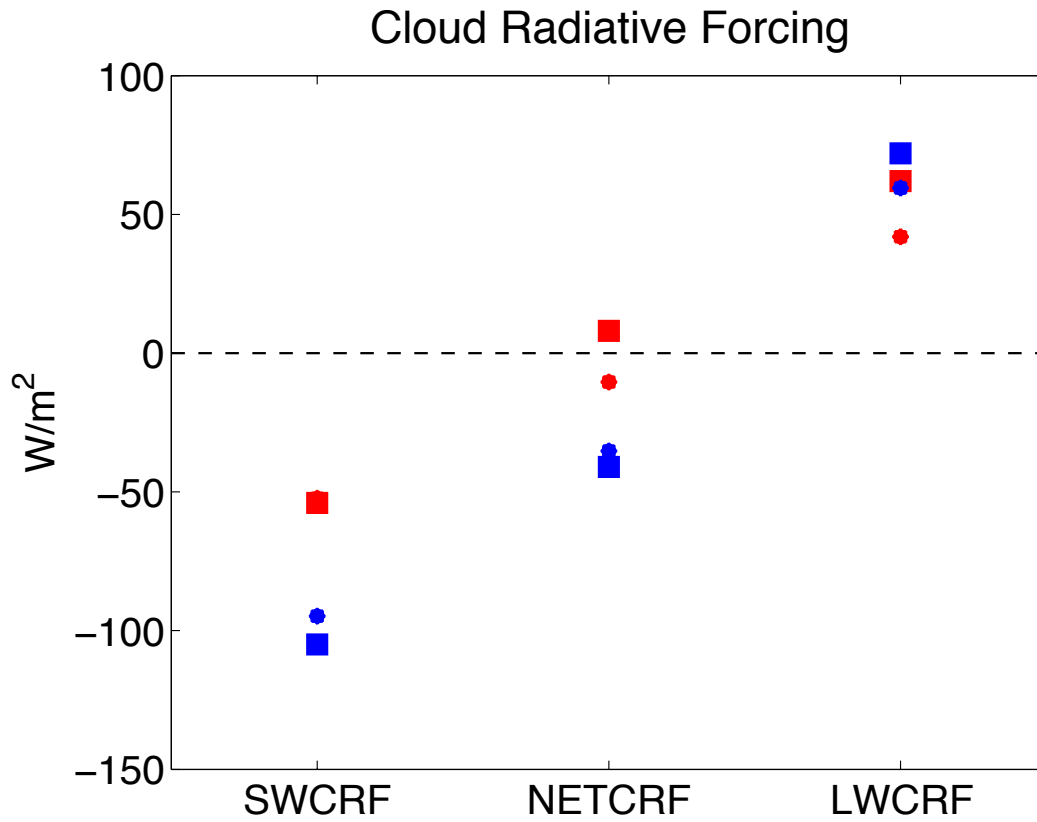
436 Fig.4. Diurnal cycle of (a) latent heat flux, and (b) net shortwave at the surface, for WRF
437 modeled (thick) and observed (thin) fluxes. Observed fluxes are taken from the
438 climatology of eddy-covariance fluxes observed at K34 station in Reserva Biológica do
439 Cuieiras. We note that surface observations have difficulty observing in the presence of

440 dew (eddy-covariance measurements typically cannot correctly record measurements) so
441 that the observations typically omit fog situations, with an overrepresentation of
442 relatively clear days compared to fog days.

443

444

445



446

447 Fig. 5. Cloud radiative, shortwave (SWCRF), longwave (LWCRF), and net (NETCRF)
448 for the wet (blue) and dry (red) season as simulated (in squares) and observed from
449 CERES (in circles).